



A methodology for calibrating parameters in discrete element models based on machine learning surrogates

Joaquín Irazábal¹ · Fernando Salazar¹ · David J. Vicente¹

Received: 28 June 2022 / Revised: 28 November 2022 / Accepted: 17 December 2022 / Published online: 5 January 2023
 © The Author(s) under exclusive licence to OWZ 2023

Abstract



The discrete element method (DEM) is well suited for calculating the behaviour of bulk materials. However, its application is limited because of the cumbersome calibration process required. Trial and error calibration can be useful for the computation of single outputs, but is unfeasible when the aim is reproducing more complex phenomena with high accuracy. This paper describes an iterative procedure based on machine learning to automatically calibrate the parameters of DEM models for reproducing the behaviour of bulk materials. The performance of the methodology is assessed by its application to the calibration of a DEM model to compute the stress–strain evolution of a cohesive material under uniaxial compression. In this case, a random forest model is used in conjunction with the iterative calibration algorithm proposed. The results of this study show that the algorithm is accurate and flexible for the calibration of material parameters.

Keywords Calibration bulk materials · Discrete element method · Machine learning · Random forest · Surrogate model

Abbreviations

DEM	Discrete element method	y_{DEM}	DEM result
DE	Discrete element	I_e	Initial absolute error for the calibration algorithm
ML	Machine learning	L_s	Number of predictions in each iteration for the calibration algorithm
RF	Random forests	it_{max}	Maximum number of iterations for the calibration algorithm
RT	Regression trees	it	Iteration
DOE	Design of experiments	DMT	Derjaguin-Muller-Toporov contact model
AOR	Angle of repose	JKR	Johnson-Kendall-Roberts contact model
QoI	Quantity of interest	H^2	Double hierarchy method
LHS	Latin hypercube sampling	X_{pred}	Combinations of parameters for each iteration of the calibration algorithm
NN	Neural network	δ	Overlap between DEM particles
OOB	Out-of-bag	\mathbf{x}	Position of DEM particles
VIMP	Variable importance	r	Radii of DEM particles
R^2	Coefficient of determination	F_N	Normal contact force between DEM particles
MAE	Mean absolute error	k_N	Normal stiffness of the contact between DEM particles
n	Number of DEM parameters to calibrate	d_N	Normal damping coefficient between DEM particles
p_i	Value of the parameter i	γ	Fraction of the critical damping
N	Number of numerical calculations for creating the training set	F_T	Tangential contact force between DEM particles
m	Number of elements in the vector QoIs	k_T	Tangential stiffness of the contact between DEM particles
err	Target variable		
y_{lab}	Laboratory measurement		

✉ Joaquín Irazábal
 jirazabal@cimne.upc.edu

¹ International Center for Numerical Methods in Engineering (CIMNE), Barcelona, Spain

d_T	Tangential damping coefficient between DEM particles
ξ	Relative displacement of the contact point parallel to the contact surface between DEM particles
F_c	Cohesive contact force between DEM particles
\hat{E}	Equivalent Young modulus of the contact between DEM particles
A	Contact area between DEM particles
l	Contact length between DEM particles
\hat{c}	Cohesive stress between DEM particles
σ_N	Compressive stress between DEM particles
E	Young modulus
ν	Poisson ratio
μ	Friction
c_{\max}	Maximum cohesion
c_0	Initial cohesion
k_c	Amount of cohesion from stress
COR	Coefficient of restitution

1 Introduction



The discrete element method (DEM) [15] is appropriate for the calculation of bulk materials [13] which typically undergo significant local deformation. Continuum-based techniques can also be applied, but they require complex elasto-plastic constitutive laws and do not adequately describe basic bulk behaviour, such as nonlinear deformations and local yielding [45]. The DEM also has the advantage of being able to provide dynamic information, such as particle trajectories and transient forces, which can not be obtained using continuum-based methods [75].

This numerical method can also be very useful in the evaluation of the behaviour of cohesive [43,54,60] and continuous media [9,51] since breakage and cracking can be modelled in an efficient way. One of the main limitations of the method is the need to calibrate the parameters that define the contact model, which lack a straightforward relation with any specific physical property. A clear example is the use of rolling friction to simulate the irregular shape of non-spherical particles with spheres. Rolling friction consists of applying a rotational frictional torque to inhibit particle rotation [74] and does not explicitly correspond to any physical property of the granular material.

Calibration is also essential when the coarse grain approach needs to be applied [14,31,44,59]. This implies increasing the diameters of the particles beyond their physical values to reduce the computational cost: each particle in the DEM model represents a group of actual particles. The input parameters for coarse grain simulations cannot be derived directly from the laboratory tests either [57].

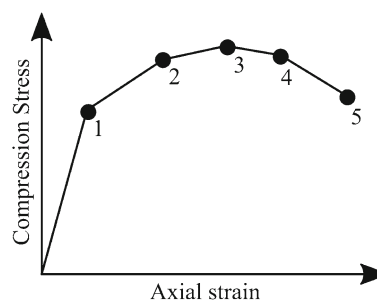


Fig. 1 Characteristic shape of stress–strain curves from uniaxial compression tests

Computational time in DEM simulations is strongly dependent on the shape of the particles, which condition the complexity of the contact search and its resolution. Among other alternatives, such as polyhedrons or clusters of spheres, the most popular and efficient simplification is the use of spherical particles [75]. This geometrical idealization affects the contact mechanism and adds complexity to the calibration process.

Trial and error is still widely used for the calibration of DEM parameters, despite its inefficiency [58,70]. The amount of parameters to calibrate depends on the contact model considered. In many settings, their influence on the results and their possible interaction is unclear. This is even more challenging when dealing with nonlinear multiple outputs (Fig. 1) instead of scalar values.

The difficulty in calibrating DEM parameters has resulted in the proposal of different methods [13]. Since computational cost is always an issue when modelling granular materials with the DEM, the calibration strategies focus on reducing the overall amount of simulations to perform. This is done basically with two approaches:

- Applying some procedure for smart updating of the model parameters, so that acceptable values are obtained with admissible number of iterations of the DEM.
- Using some simplified reduced order model (often called surrogate model) with low computational cost in combination with the full DEM simulations.

Among those using the first option, Yoon [70] presented a methodology using Design of Experiments (DOE) and optimization techniques aiming to decrease the number of necessary DEM calculations for the calibration of uniaxial compression simulation of rocks. In the same line, Boikov et al. [4] applied DOE with an iterative algorithm to calibrate the flow rate and Angle of Repose (AOR) of a generic bulk material, while Zhang et al. [72] used DOE for calibrating the AOR of rice grains.

Hlosta et al. [33] calibrated the properties of different industrial materials applying DOE for the computation of

the static and dynamic AOR. Similarly, Orefice and Khinast [53] presented a rational, automatized calibration routine. In their work, they identified the material properties with a higher influence on the results of different laboratory tests. Then, DEM calculations were performed in a specific order that allowed sequential calibration of the parameters: friction was calibrated with the AOR test, plastic stiffness with the uniaxial compression test and cohesive stiffness with the shear test. The same sequence was repeated until acceptable accuracy was obtained. Similarly, Desai et al. [20] analysed the effect of DEM parameters on the behaviour of additive manufacturing powders to simplify the calibration process.

On their part, Hanley et al. [27] applied Taguchi methods to assess the influence of the material parameters in the calculation response of bonded agglomerates. The aim of their study was to optimize the calibration procedure.

Other possibility is the use of dimensional analysis to establish the relationship between material properties and numerical parameters. This approach has been followed by Fakhimi and Villegas [23] and by Hsieh et al. [35] to characterise the microscopic properties of a synthetic material and to calibrate the material parameters of sandstones, respectively. In both studies, dimensional analysis allows not only to calibrate the material parameters, but also to better understand the relationship between each property.

The use of surrogate models based on advanced statistics or machine learning (ML) techniques is becoming popular in recent years. Once fitted, these models can be applied to compute the Quantities of Interest (QoIs) of the case at a negligible computational cost. Full DEM simulations are only necessary to create a training set large enough for the ML model to provide estimates of the full model that are sufficiently accurate. This approach benefits from the rapid advances in ML algorithms and has also been applied in combination with numerical methods in other fields [12,28]. The most relevant works related to the calibration of DEM parameters using this approach are briefly summarized in the following paragraphs.

Do et al. [21] applied genetic algorithms to the calibration of the material properties of quartz sand. They calibrated the bulk density, AOR, and discharging time in an hourglass test. The calibration process searches for the input parameter set whose simulation produces the best match of the three simulated outputs with the experimental measurements.

Rackl and Hanley [57] described a calibration approach based on Latin Hypercube Sampling (LHS) and Kriging that was applied to estimate the AOR and bulk density for spherical glass beads. A reduced number of DEM calculations are required to fit the Kriging metamodel, which is later applied to calibrate: the Young modulus, the sliding and rolling friction, the density and the time step, aiming to reduce the computational time. Grobber et al. [26] presented a similar approach also based on LHS and Kriging for calibrating

six DEM parameters: the sliding and rolling friction coefficients between particles with an AOR test, the sliding and rolling friction coefficients between particles and walls with an AOR test over a horizontal surface and the restitution coefficients between particles and between particles and walls with a plate impact experiment. LHS and Kriging were also applied together by De Pue et al. [18] to calibrate the DEM material parameters (Young modulus, Poisson ratio, the friction angle and normal and shear cohesion) to reproduce the stress–strain behaviour of unsaturated soils during uniaxial compression.

Westbrink et al. [68] proposed a calibration procedure with parameter optimization based on multi-objective reinforcement learning. The results of two different experiments are considered to train an agent to find a suitable material parameter set. The QoIs are the static and dynamic AOR of the material. They validated the model by calibrating three different materials: a plastic granulate, wood pellets and wet sand.

Cheng et al. [11] calibrated four micromechanical parameters of glass bead packing under oedometric compression. They described a methodology based on an iterative Bayesian filtering framework trained with DEM parameters to compare the porosity, mean stress and deviatoric stress ratio obtained in the laboratory and in the numerical calculations. In their work, the initial configuration of the laboratory test, including the position of the particles, is known. Each iteration involves 100 DEM calculations decreasing the intervals of the parameters. Based on this work, Hartmann et al. [30] presented a comprehensive study on the performance of iterative Bayesian filtering for the calibration of DEM models based on triaxial compression tests.

Mohajeri et al. [48] developed an iterative automated calibration procedure, based on the Non-dominated Sorting Genetic Algorithm. To assess its performance, they reproduced the measured shear stresses of a cohesive coal sample at two different pre-consolidation levels.

El-Kassem et al. [22] applied DOE together with Multivariate Regression Analysis. They focussed on the impact of six DEM input parameters (coefficients of static and rolling friction, coefficient of restitution, particle size, Young's modulus and cohesion energy density) on five output responses (angle of repose, porosity, mass flow rate, translational kinetic energy and computation time) in AOR tests applied to free-flowing and cohesive powders.

Zhang et al. [71] presented a calibration methodology where the nonlinear relationship between macroscopic responses and microscopic parameters is obtained using the response surface method. They used the DEM for simulating a large-scale triaxial compression test of rockfill materials.

Benvenuti et al. [3] proposed a calibration method based on neural networks (NNs). They carried out several calculations of Schulze shear cell tests [62] and AOR tests with the

DEM to reproduce the internal friction and the AOR obtained in laboratory tests. Since the NN model is fit to approximate the differences between DEM and laboratory results, values are searched for which minimize the output of the NN model. Within the appropriate ranges, all possible combinations of 100 different values for sliding and rolling friction and 25 for coefficient of restitution and density were checked. Therefore, they evaluated 6,250,000 combinations.

Zhou et al. [73] presented a similar calibration procedure based also on NNs. They calibrated the particle density, sliding frictions, coefficients of restitution and Poisson's ratio of expanded graphite by analysing the angle of repose and bulk density. Likewise, Ye et al. [69] used NNs to calibrate the shear, static and dynamic AOR by reproducing a draw-down and a rotating drum experiment.

With the objective of reducing the computational time required for the calibration procedure, Fathipour-Azar [24] analysed several ML algorithms to estimate the preliminary value of the material parameters prior to calibration.

In view of the profusion of publications on the topic, Richter et al. [58] proposed a general, high-level framework and terminology for DEM calibration based on surrogate models that they called *Generalized Surrogate Modelling-based Calibration*. They describe the elements of these approaches: a) Sampling strategy; b) Objective function; c) Stopping criterion and d) Adaptive sampling strategy. The case study chosen involves only two DEM parameters.

In this work, an innovative calibration procedure is proposed. As other methods based on surrogate modelling, it can be considered as a particularization of the general framework described by Richter et al. [58]. The main difference of this approach is that it can be applied in complex settings: with many DEM parameters to calibrate problems with multiple outputs (vector QoIs), such as stress–strain curves, very common in DEM calculations [29,38].

Although the overall approach can be used with different ML algorithms, here we use random forests (RF), which provides additional advantages: a) the importance of the inputs, which can be used for variable selection, is automatically computed during model training [5]; b) the accuracy of the surrogate model can be evaluated using all initial DEM simulations without the need for using an external data set by estimating the Out-of-Bag (OOB) error.

The method also allows reusing the DEM calculations for calibrating other materials of the same nature.

The document is structured as follows: firstly, the calibration algorithm is described in Sect. 2. Then, a specific implementation is described in Sect. 3 with an example of application. The results are presented in Sect. 4 and discussed in Sect. 5. Finally, Sect. 6 includes some conclusions.

2 Calibration procedure

The proposed methodology is based on a ML-based meta-model. The overall strategy thus involves two main steps: the development of the metamodel, which requires running a set of DEM simulations, and its application for obtaining the calibrated parameters. They are both described in this section.

2.1 Overview of the calibration methodology

The high-level scheme of the calibration methodology is shown in Fig. 2, with focus on the steps to be followed for developing the surrogate model. First, the n DEM parameters to calibrate need to be identified, and the corresponding initial ranges defined ($[p_i^{\min}, p_i^{\max}] \forall i \in [1, n]$). In parallel, the QoIs of the phenomenon need also to be specified. The approach is devised for vector QoIs including m elements. In the case study selected, such elements correspond to m points in the stress–strain curve measured during a uniaxial compression test (Fig. 1).

The next decision to be made is the number (N) of numerical calculations to perform to create the training set for the surrogate model. The accuracy of the surrogate model increases with the size of the training data [58], but computational cost is typically high in DEM simulations. The choice of N shall thus depend on the computational cost of each individual run of the DEM and on the overall time schedule. In the proposed approach, LHS is used for generating the input values for the N combinations considered. LHS is a pseudo-random sampling method in which the range of variation in each parameter is divided into a number of intervals. The value of each parameter is taken randomly from a different interval for each combination, with the aim of increasing the variety of the samples for a given number of realizations [26,69].

The results of the N DEM models are used to create the training datasets for fitting the surrogate model. In particular, we create m training sets for fitting m surrogate models. All training sets have the same input data (the n parameters to calibrate) and differ in the target variable (err), which is taken as the difference between the DEM model and the experimental result, as shown in Eq. 1:

$$\begin{aligned} err_j^k &= y_{lab}^k - y_{DEM,j}^k = f(p_i) \\ \forall k \in [1, m], \forall j \in [1, N]; \text{ and } \forall i \in [1, n] \end{aligned} \quad (1)$$

where y_{lab} is the laboratory measurement and y_{DEM} is the DEM result. Therefore, in the case study, for each degree of axial strain in the stress–strain curve, the surrogate models approximate the error obtained with a DEM model as a function of the DEM parameters to calibrate.

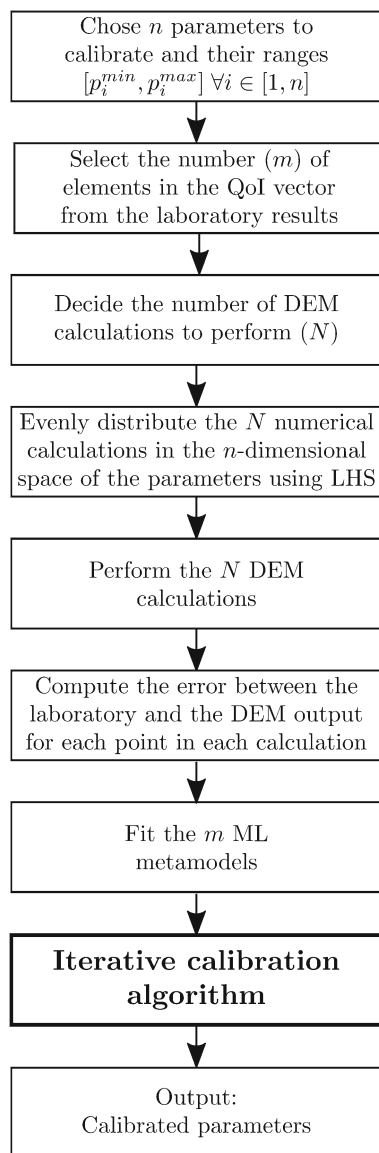


Fig. 2 Scheme of the calibration procedure

This part of the methodology is highly general and can be applied in combination with any algorithm for generating the surrogate model.

2.2 Iterative calibration algorithm

Once a surrogate model is available to approximate the error of the full DEM model, it can be applied for calibrating the parameters with low computational cost. In this section, an iterative algorithm is described for this purpose. The overall strategy involves defining some initial (wide) ranges for the parameters to calibrate, which are narrowed at each iteration until some stopping criterion is reached. The final calibrated parameters are taken as the median values of the ranges

obtained in the last iteration. The steps are described in more detail in the following subsections.

2.2.1 Algorithm parameters

The specific parameters of the calibration procedure are

- *Initial absolute error (I_e)*: maximum admissible absolute value for the outcome of the surrogate models in the first iteration. It should be reminded that the target value of the ML models is the difference between DEM and laboratory results (see Eq. 1). The admissible error for each iteration it is computed as I_e/it .
- *Number of predictions in each iteration (L_s)*: number of evaluations of the ML model to be performed at each iteration. Each evaluation is made on a combination of values for the parameters to calibrate generated with the LHS method.
- *Maximum number of iterations (it_{max})*: maximum number of iterations (it) for the algorithm to complete the execution.

2.2.2 Algorithm scheme

Figure 3 shows the structure of the algorithm, which includes the following steps:

1. *Initialize the algorithm* the initial values of the algorithm parameters (I_e , L_s and it_{max}) and the material parameters ($[p_i^{min}, p_i^{max}]$) are set.
2. *Create a set of combinations of parameters* X_{pred} a matrix of size L_s is created applying the LHS method and the ranges defined for the corresponding iteration (either the initial or updated ranges).
3. *Update ranges* the predictions of the ML models (ML^k) are computed for the L_s samples and each of the m elements in the QoI vector. Valid combinations of parameters include those with estimated error below I_e/it for all m . New ranges are defined from the maximum and minimum values of the valid combinations for each parameter.
4. *Stopping criterion* the calculation finishes either when it_{max} is achieved or when none of the combinations of parameters meet the admissible error for the new iteration (all combinations lead to $err > I_e/it$).
5. *Final parameters* the final values are computed as the median of the final ranges obtained after the iterative process.

To better illustrate the algorithm, Fig. 4 shows graphically an example of calibration with two QoIs (m_1 and m_2), one

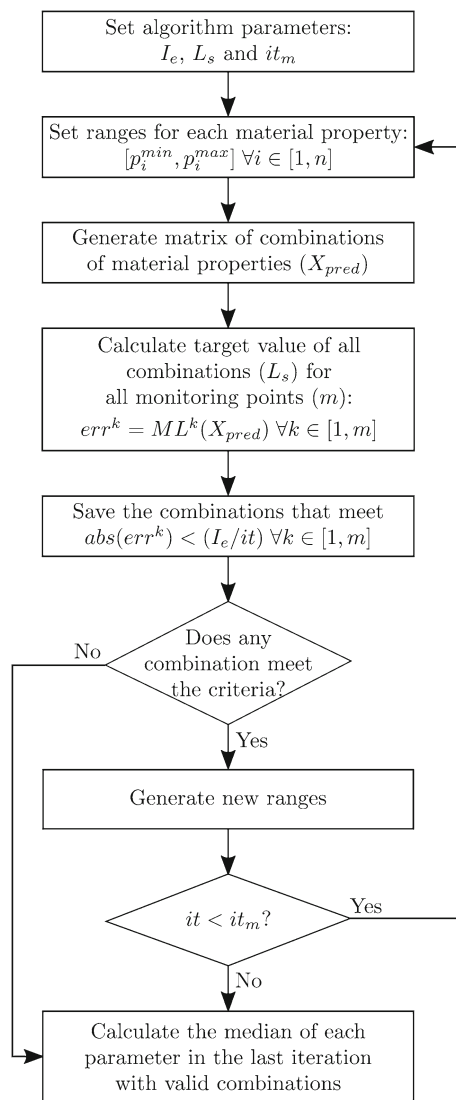


Fig. 3 Scheme of the algorithm

material parameter (p_1), three iterations ($it_{max} = 3$) and ten combinations of parameters ($L_s = 10$).

The graphs in Fig. 4 display p_1 on the x -axis and the error predicted by the ML model in m_1 and m_2 on the y -axis. In the first iteration, the values of p_1 are evenly distributed over the *Initial Range*. Then, the initial error (I_e) is plotted. In the example, the error is lower than I_e for all p_1 . As a result, the ranges for p_1 remain unchanged for iteration 2. However, the permissible error for $it = 2$ is $I_e/2$, which results in not valid values of p_1 and in turn in reduced range. In the last iteration, a new group of values for p_1 are generated over the *New Range*, resulting in a more dense distribution (same number of samples L_s , narrower range). The permissible error decreases again to $I_e/3$ and the p_1 range also decreases. After the last iteration, the median of the value of p_1 is chosen as the calibrated result.

3 Application of the calibration procedure

The calibration procedure has been applied to the simulation of a clay specimen subjected to a uniaxial compression test. The behaviour of this material has been reproduced with a cohesive DEM model based on the work of Obermayr et al. [52], implemented in the Kratos Multiphysics framework [17].

The DEM code is first used to perform the initial set of N simulations with different material parameters to fit the ML surrogate model (Fig. 2). The multidimensional distribution of these parameters was generated with the LHS method optimized using the maximin-criterion [42], which allows the assignment of parameters in a near-random sample pattern. For this application, the surrogate model is based on RF, a ML algorithm with useful characteristics for this problem, as described in Sect. 3.3.

3.1 Laboratory experiments

The clay sample was prepared according to the standard UNE 103400:1993 [1], with 2000 g of sand and 500 g of bentonite [49]. While the humidity of the sand is zero, the bentonite contained a 13.8% of water. The humidity of the mixture is 17.4%. Figure 5 shows the layout and the geometry of the simple compression test carried out.

Figure 6 shows the compression stress vs axial strain curve obtained in the laboratory. In the experiment, the compression stress was registered for 17 equispaced values of the axial strain of the specimen ($m = 17$), from the initial state to a maximum value of 11.33%.

3.2 Discrete element model with stress-dependent cohesive contact

The cohesive DEM contact model applied in this work is derived from the classical linear spring-dashpot model [16] for cohesionless material with spherical particles. Cohesion is modelled by adding a normal attractive force between the particles. This contact law depends on the stress history, since the amount of cohesion is limited by the contact pressure applied during the calculation and is based on the work of Obermayr et al. [52] (scale invariant model in the quasi-static regime [25]).

The normal force is computed as a function of the overlap δ_{ij} between particles i and j , which depends on their locations \mathbf{x}_i and \mathbf{x}_j and their radii r_i and r_j

$$\delta_{ij} = r_i + r_j - \|\mathbf{x}_i - \mathbf{x}_j\| \quad (2)$$

When $\delta_{ij} < 0$, the contact force ($F_{N,ij}$)—normal to the contact surface—is calculated by applying a linear spring-dashpot model. Moreover, cohesion is activated when two

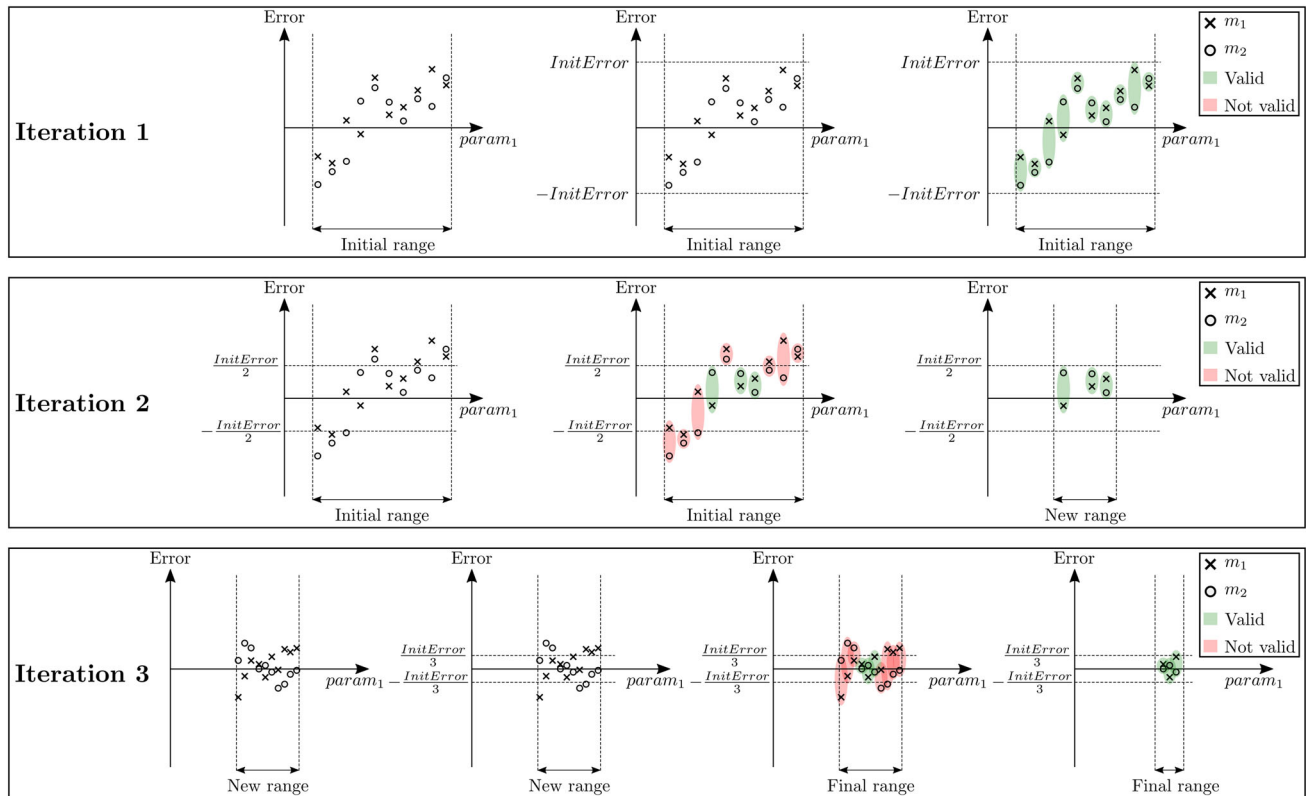


Fig. 4 Graphical example of the calibration procedure with two elements in the QoI vector (m_1 and m_2), one material parameter (p_1), three iterations ($it_{max} = 3$) and ten combinations of parameters ($L_s = 10$)

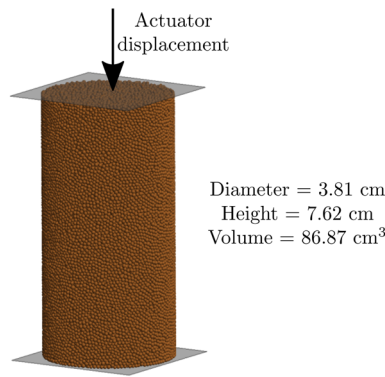


Fig. 5 Geometry of the specimen

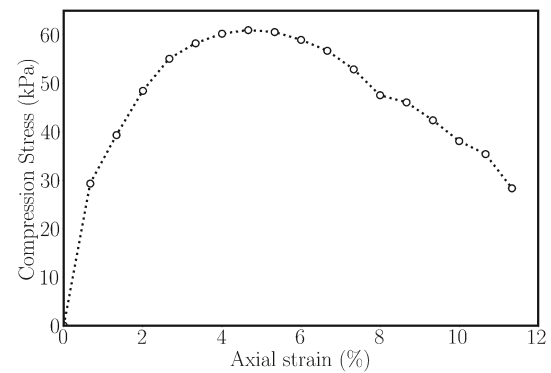


Fig. 6 Laboratory results

particles are in contact. With the cohesive model, the normal force is calculated as

$$F_{N,ij} = k_{N,ij} \cdot \delta_{ij} + d_{N,ij} \cdot \dot{\delta}_{ij} + F_{c,ij} \quad (3)$$

where $F_{c,ij}$ is the cohesive contact force, $k_{N,ij}$ is the normal stiffness of the contact and $d_{N,ij}$ is the damping coefficient.

$k_{N,ij}$ is computed as

$$k_{N,ij} = \frac{\hat{E} A_{ij}}{l_{ij}} \quad (4)$$

where \hat{E} is the equivalent Young modulus ($\hat{E} = \frac{E_i E_j}{E_i + E_j}$), A_{ij} is the contact area and l_{ij} is the contact length.

$d_{N,ij}$ is taken as a fraction γ of the critical damping (c_c)

$$d_{N,ij} = \gamma c_c = 2\gamma \sqrt{\hat{m} k_{N,ij}} \quad (5)$$

Assuming that the mass of the contacting particles is m_i and m_j , the equivalent mass (\hat{m}) is

$$\hat{m} = \frac{m_i m_j}{m_i + m_j} \quad (6)$$

γ is related with the coefficient of restitution (COR)—a fractional value representing the ratio of speeds after and before an impact—through the following expression [50]:

$$\gamma = \frac{-\ln(\text{COR})}{\sqrt{\pi^2 + (\ln(\text{COR}))^2}} \quad (7)$$

Obermayr et al. [52] calculated the contact length as

$$l_{ij} = r_i + r_j \quad (8)$$

and the contact area as

$$A_{ij} = \pi \cdot r_{ij}^2 \quad (9)$$

while we calculated them as

$$l_{ij} = r_i + r_j - \delta_{ij} \quad (10)$$

$$A_{ij} = \pi \cdot r_{ij}^2 \frac{r_i + r_j}{r_i + r_j - \delta_{ij}} \quad (11)$$

where $r_{ij} = \frac{r_i + r_j}{2}$.

Therefore, in our model, the stiffness of the contact increases with the indentation between particles, as in the well-known DMT [19] and JKR [41] cohesive contact models.

The cohesive force from Eq. 3 depends on the cohesive stress (\hat{c}_{ij}) and A_{ij} and is computed as

$$F_{c,ij} = \hat{c}_{ij} \cdot A_{ij} \quad (12)$$

If the cohesive stress was constant, this contact model would be similar to the DMT model, leading to a problem of excessive cohesion in the new contacts formed (all the attractive force between the particles would be activated at the same time when the particles come into contact). To avoid this problem, the cohesive stress has been modified to consider the maximum compressive stress to which each contact has been subjected during the calculation.

An initial cohesive stress, equal to the initial cohesion ($\hat{c}_{ij} = c_0$), is applied to the contacts existing at the beginning of the calculation. In successive time steps, the new or reactivated contact pairs start with a null cohesive stress ($\hat{c}_{ij} = 0$) that increase depending on the compressive stress to which each of the contacts is subjected:

$$\sigma_{N,ij} = \frac{F_{N,ij}}{A_{ij}} \quad (13)$$

the cohesive stress is calculated as

$$\hat{c}_{ij} = k_c \cdot \max(\sigma_{N,ij}^{(t=1)}, \sigma_{N,ij}^{(t=2)}, \dots, \sigma_{N,ij}^{(t=nt-1)}) \quad (14)$$

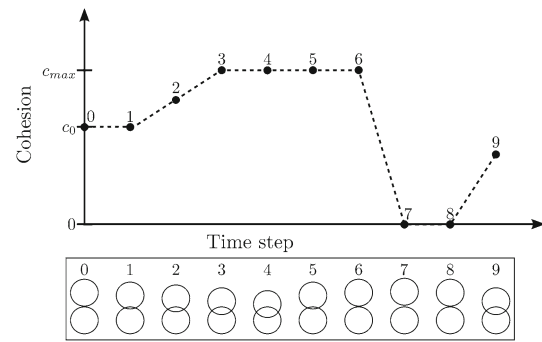


Fig. 7 Diagram showing the relation between cohesion and time history of indentation between two particles

k_c being a material parameter known as the amount of cohesion from stress and nt being the time step.

The cohesive stress is limited by the maximum cohesion c_{\max} , another material parameter. As a result, the cohesive stress depends on three parameters (c_0 , k_c and c_{\max}), is different for each contact and is updated every time step $\hat{c}_{ij}^{t=nt}$.

The relation between cohesion and time history of indentation is illustrated in Fig. 7 for two particles initially in contact, which first approach and later separate. Initial cohesion ($\hat{c}^{t=0}$) equals c_0 . In the first time step, indentation increases but $k_c \cdot \max(\sigma_N^{(t=0)}, \sigma_N^{(t=1)}) < c_0$, therefore, $\hat{c}^{(t=1)} = c_0$; in the second time step, $c_0 < k_c \cdot \max(\sigma_N^{(t=0)}, \dots, \sigma_N^{(t=2)}) < c_{\max}$, hence, $\hat{c}^{(t=2)} = k_c \cdot \max(\sigma_N^{(t=0)}, \dots, \sigma_N^{(t=2)})$; next, $k_c \cdot \max(\sigma_N^{(t=0)}, \dots, \sigma_N^{(t=nt)}) > c_{\max}$, for $nt = (3, 4)$ so $\hat{c}^{(t=3)} = \hat{c}^{(t=4)} = c_{\max}$. Indentation decreases for $nt = 5$ and 6, but $\hat{c}^{t=nt} = c_{\max}$ because of the previous values. Finally, particles detach in time step 7 ($\delta_{ij} > 0$), and thus, $\hat{c}^{t=nt} = 0$ and the stress history is erased. If the contact is activated later in the simulation, $\hat{c}^{t=nt} = \min(k_c \cdot \max(\sigma_N^{(t=0)}, \dots, \sigma_N^{(t=nt)}), c_{\max})$.

The tangential contact force $F_{T,ij}$ is calculated through a regularized Coulomb model [56]. The update of the tangential force at time step $(n + 1)$ reads

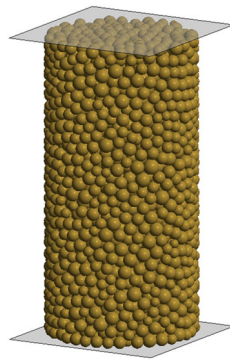
$$F_{T,ij}^{(n+1)} = F_{T,ij}^n + k_{T,ij} \cdot \Delta \xi_{ij}^{(n+1)} + d_{T,ij} \cdot \dot{\xi}_{ij} \quad (15)$$

- where $k_{T,ij}$ is the tangential contact stiffness, $d_{T,ij}$ is the damping coefficient and ξ_{ij} the relative displacement of the contact point parallel to the contact surface.

Maw et al. [46] introduced the following relation between the tangential and the normal stiffness ($\kappa = \frac{k_T}{k_N}$) [65]:

$$\kappa = \frac{2(1 - \nu)}{2 - \nu} \quad (16)$$

being ν the Poisson coefficient.

Fig. 8 Spheres mesh used in the DEM calculations

The damping coefficient in the tangential direction is also taken as a fraction γ of the critical damping (c_c)

$$d_{T,ij} = \gamma c_c = 2\gamma \sqrt{\hat{m}k_{T,ij}} \quad (17)$$

If the tangential force exceeds the limit $F_{T,ij} > \mu F_{N,ij}$, where μ is the local friction coefficient, slipping friction occurs.

Regarding particle rotation, Obermayr et al. [52] applied a very high rolling resistance coefficient (0.99), as the behaviour of clay specimen is mainly driven by the cohesion [47]. This high value of the rolling resistance parameter restricted the rotation almost completely. In this work, we assume that the DEM particles do not rotate.

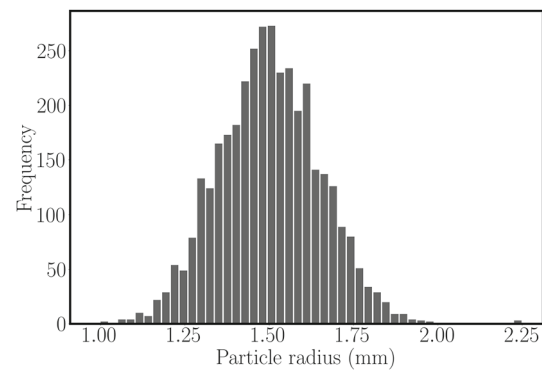
3.2.1 Size and distribution of the spherical particles

Coarse grain approach is compulsory when using DEM to reproduce clay materials, since the particle size of clay is around 10^{-3} mm. We used an average radius of the spherical DEM particles of 1.5 mm. This size has been chosen to ensure that the specimen is at least ten times larger than particle size in all lengths (height, width and length) [37]. The goal is to minimize the influence of contours and boundaries as much as possible.

The initial configuration of the DEM model was generated with the gravitational packing technique [66]: GiD spheres mesher [67] is first used for filling a confining cylinder larger than the test specimen. Then, a pre-simulation with particles with null friction is run. During the pre-simulation, the force of gravity is allowed to act, the particles accommodate and a well-compacted sample is obtained.

The final model is composed of 3686 spheres (Fig. 8), resulting in a packing fraction of 61.74%, which can be considered adequate [2,64] (for instance, Orefice et al. [53] used a model with packing fraction lower than 60%).

Figure 9 shows the particle size distribution, with radii ranging from 0.97 to 2.25 mm and a standard deviation of 0.15 mm.

**Fig. 9** Particle size distribution**Table 1** Range of the material properties used in the DEM calculations.

Property	Range
Young modulus (E) [MPa]	[2.50 – 10.00]
Poisson ratio (ν)	[0.01 – 0.49]
Friction (μ)	[0.25 – 0.50]
Maximum cohesion (c_{\max}) [kPa]	[30.00 – 100.00]
Initial cohesion (c_0) [kPa]	[10.00 – 30.00]
Amount of cohesion from stress (k_c)	[0.01 – 0.50]
Coefficient of restitution (COR)	[0.01 – 0.99]

3.2.2 Model parameters

The constitutive model used in this work involves eight material properties that have to be defined. The density can be directly taken from the experiments, being 3280 kg/m^3 .

Thus, we have seven unknown parameters that need to be calibrated ($n = 7$). The initial ranges of variation in these parameters are presented in Table 1. They were selected from the bibliography and experience in previous calculations.

The contact between the particles and the contours (actuators of the laboratory device) is calculated by the Double Hierarchy method (H^2) [61]. It is assumed that the parameters that characterise the contact between the material and the actuators do not significantly influence the results, thus the same parameters were used for particle-particle and wall-particle contacts.

3.2.3 Other computational considerations

We use a Velocity Verlet scheme for integrating the translational motion [39]. This integration scheme, together with the material parameters and particles size, allowed us to apply a numerical time step of 10^{-6} seconds.

In an effort to reduce the overall computational time, and in view of the results of preliminary simulations, the application

of the load in the DEM model was accelerated 600 times as compared to the laboratory tests.

3.3 ML model

The designed calibration procedure can be performed with different ML models, such as NNs or different Tree-based methods. In this work, we chose the RF model [7,40], an algorithm that has shown to be robust and easy to implement in previous works [10,36]. RF belongs to the family of ensemble methods, because the final prediction is computed from a high number of simple models. In the case of RFs, the base models are regression trees, whose predictions are averaged to obtain the overall output [8]. Regression trees (RT) are based on the division of the input space into homogeneous regions. The prediction of the RT model is a set of constant values, equal to the average of the observations included in each region. These models are easy to interpret, but their accuracy is in general low. RF models make use of the advantages of RTs and overcome their drawbacks by means of an optimized strategy for maximizing prediction accuracy of the ensemble.

In particular, two random components are included:

1. Each tree in the forest is fitted on a randomly modified version of the training set (bootstrap sample), in which some of the training samples appear once, some are duplicated and others are excluded.
2. A random subsample of the input variables is considered for defining each split of each tree. This allows capturing the contribution of secondary inputs.

RF models keep the benefits of regression trees, such as high execution speed, easy usage, and no need of scaling or preprocessing data. Moreover, RF corrects the low accuracy and generalization capability of regression trees in front of unseen data (overfitting) if they are grown to arbitrary complexity [34].

In this work, we used the RF tool available in *Scikit-learn* [55] for regression. *Scikit-learn* is a ML library for the Python programming language.

In addition to the advantages already mentioned, the RF regressors are robust, i.e. the model parameters have low influence on the results, which simplifies the fitting process. Further advantages of the algorithm include

1. The importance of the inputs is automatically computed during training. This can be used to remove some of the parameters from the calibration process.
2. The model accuracy can be reliably computed using the samples excluded from each bootstrap sample. This is called the OOB accuracy and allows using all the available data for model fitting.

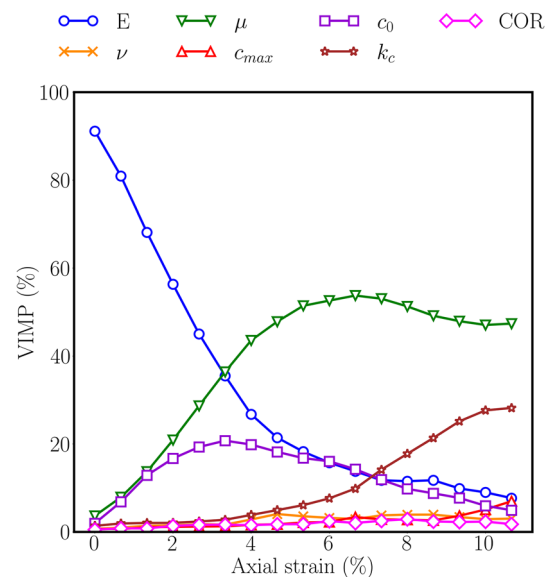


Fig. 10 Percentage of the importance of each material property as a function of the axial strain

3.3.1 Fitting process

In this example, initially, 100 DEM calculations were performed to fit the RF metamodel ($N = 100$). The default parameters of the *RandomForestRegressor* function available in *Scikit-learn* were applied in this work: 500 trees in the ensemble and one third of the inputs considered at each split.

3.3.2 Variables importance and variables selection in RF models

The influence of the input variables in a RF model is automatically computed during model fitting. Figure 10 shows the results for the initial seven material parameters considered and the 17 outputs (points in the stress–strain curve). These results thus come from the analysis of the RF model fitted to the training data (generated with the DEM).

It can be noticed that while the axial strain of the specimen is small and mainly elastic, the process is mostly governed by the Young modulus E ; however, as the specimen deforms, the importance of E decreases and that of other properties increases. This is the case, for instance, of μ , which shows low relevance in the first instants of the calculation but increases as the frictional forces start to act. As the axial strain advances, the particles begin to slide over each other and the importance of μ remains almost constant until the end of the test.

As for the cohesive parameters, c_0 is more important in the first half of the calculation, while k_c is more relevant in the second part. This is explained because as the contact forces

Table 2 Mean VIMP of the variables

Property	Mean VIMP (%)
E	31.45
ν	2.67
μ	38.61
c_{\max}	2.42
c_0	12.51
k_c	10.54
COR	1.79

between particles develop, the cohesion increases driven by the compressive stress and k_c .

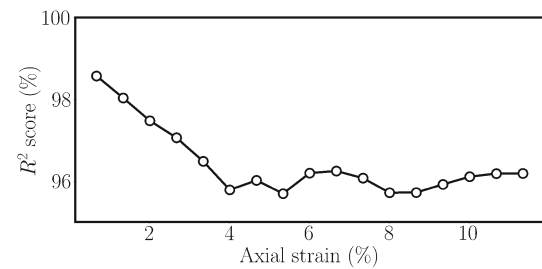
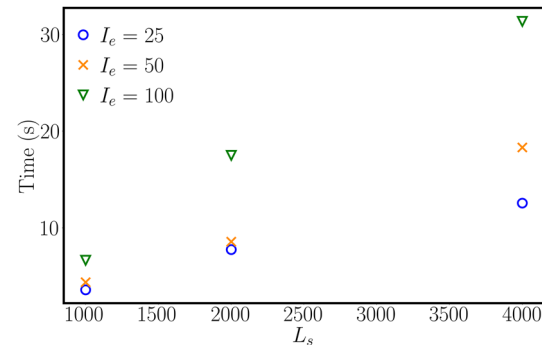
Another interesting conclusion that can be drawn from the results shown in Fig. 10 is that ν , c_{\max} and COR do not have a significant influence in the process, being their mean Variable Importance (VIMP) lower than 2.70% (see Table 2). Evaluating each point separately, the VIMP of those variables is always lower than the 7%. The low importance of ν and COR was expected for this kind of calculation, but the analysis of the RF model shows that c_{\max} does not affect the results either: the cohesion is controlled by c_0 and k_c in this test. Therefore, these three parameters were removed from the calibration. A new set of calculations was performed fixing these three properties: 0.25 for the Poisson ratio [6], 80 kPa for c_{\max} [52] and 0.02 for the COR [52].

The model accuracy was evaluated using the OOB Coefficient of Determination (R^2) score (Eq. 18) of the training data samples

$$R^2 = 1 - \frac{\sum_{i=1}^{n'} (y_i - y_i^{\text{pred}})^2}{\sum_{i=1}^{n'} (y_i - \bar{y})^2} \quad \text{with } \bar{y} = \frac{1}{n'} \sum_{i=1}^{n'} y_i \quad (18)$$

The initial data set ($N = 100$) led to a not significantly accurate RF model as the OOB R^2 score in some of the 17 outputs is about 66%. However, it helped us to exclude three unimportant parameters from the calibration process which was then run for E, μ , c_0 and k_c ($n = 4$). Moreover, the number of DEM calculations was increased to 600 ($N = 600$). The benefits of removing these uninformative variables from the calibration and increasing the number of DEM calculations are shown in Fig. 11: the OOB R^2 score is higher than 95% for all points.

Although the OOB accuracy corresponds to the entire variation in the inputs, the application of the RF models during calibration was restricted to a reduced range: the upper and lower 5% of the ranges was removed. This ensures that predictions are made within the ranges of the training set of the RF model, thus avoiding the lack of accuracy of these models when extrapolating [32].

**Fig. 11** OOB R^2 score as a function of the axial strain with $N = 600$ and $n = 4$ **Fig. 12** Computational time of the calibration algorithm for different configurations

4 Results of the calibration

The performance of the methodology presented in Section 2.2 was verified for the case study considered and different values of the calibration parameters: L_s : [1000, 2000, 4000]; it_{\max} : [50, 100, 200]; I_e : [25, 50, 100] kPa.

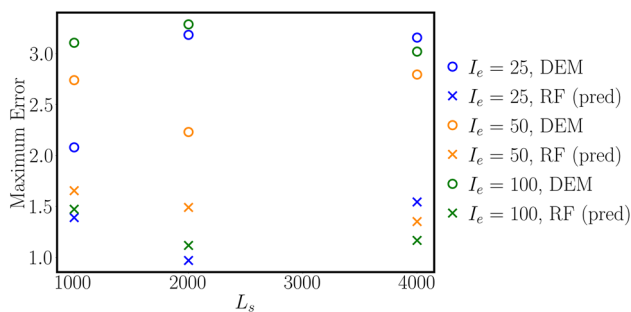
Although not used in this work, different weights can be assigned to each element in the QoI vector, resulting in different admissible error at each iteration. This can be useful for calibrating using different tests with various measuring units, e.g. when calibrating from a stress–strain curve (Pa) and the AOR (radians), or when more relevance is given to some of the outcomes (for instance, special interest in some part of the stress–strain curve).

The computational performance of the calibration algorithm was tested in one Intel(R) Core(TM) i7-6700 CPU processor. Figure 12 displays the calculation time taken for each of the parameter settings. It can be clearly seen that, as expected, the computational time increases for larger L_s . In the cases with lower I_e , the stopping criterion is met in less iterations, so the time required to calibrate is also lower. it_{\max} is not reached in any of the configurations, so, in this case, this value does not affect the computational time. The results are not plotted as they are redundant.

Nevertheless, the computational time consumed by the metamodel, regardless of the parameters used, is clearly negligible as compared to DEM. In this application, each DEM

Table 3 Calibration results for the nine calibrations performed

L_s	I_e [kPa]	E [MPa]	μ	c_0 [kPa]	k_c
1000	25	6.09	0.39	17.04	0.13
	50	6.07	0.40	16.17	0.13
	100	6.42	0.39	16.72	0.13
2000	25	6.23	0.37	19.11	0.09
	50	6.26	0.39	16.83	0.13
	100	6.34	0.37	19.04	0.11
4000	25	6.34	0.39	16.97	0.14
	50	6.26	0.40	15.75	0.15
	100	6.07	0.40	16.21	0.13
Max.		6.42	0.40	19.11	0.15
Min.		6.07	0.37	15.75	0.09

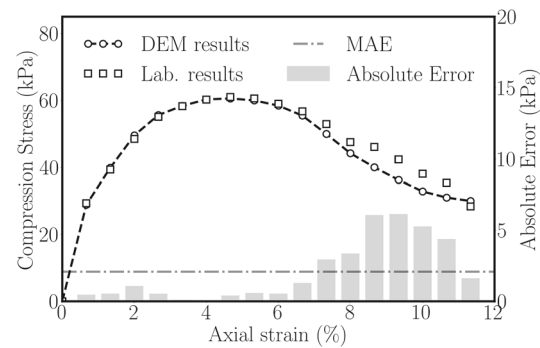
**Fig. 13** MAE obtained after applying the final parameter values to the DEM calculations and predicted by the RF model

simulation developed for fitting the surrogate model required about one hour and a half to run in 16 Intel Xeon E5-2670 CPU processors.

The results of the calibration algorithm are several combinations of parameters that are supposed to give an error lower than the value used in the last iteration (I_e/it_{last}) for all points. Then, from those combinations, we computed the median value for each material parameter. Table 3 shows the final material parameters obtained for all the cases considered. Changes in it_{max} were excluded, since this parameter had no effect in this case. With the final parameters, nine DEM calculations were performed to verify the efficiency of the process.

In Fig. 13, it can be seen that the error predicted by the RF model is always lower than the actual error obtained from the DEM calculation with the calibrated parameters. This is due to the imperfect performance of the surrogate model in predicting the response of the DEM model. Interestingly, the difference and the DEM error increase with L_s , probably due to the higher number of parameter combinations that are considered correct by the surrogate model.

From the nine calibrations performed, the best combination of calibrated parameters is corresponding to $L_s = 1000$ and $I_e = 25$ ($E = 6.09$ MPa, $\mu = 0.39$, $c_0 = 17.04$ kPa and

**Fig. 14** DEM calculation with the material properties obtained after calibrating with $L_s = 1000$, $it_{max} = 50$ and $I_e = 25$ Material parameters: $E = 6.09$ MPa, $\mu = 0.39$, $c_0 = 17.04$ kPa and $k_c = 0.13$. MAE = 2.08 kPa

$k_c = 0.13$). It provides the smaller DEM error, and it is also the one with the lowest difference between the DEM error and the error predicted by the RF model. Those parameters lead to a DEM mean absolute error (MAE) equal to 2.08 kPa.

Figure 14 shows the DEM results obtained with that combination of parameters. It can be seen that in this case, higher accuracy is obtained for the 10 first and for the last points. As mentioned before, different weights can be given to each point in the curve in case there is special interest in better capturing certain interval of the test.

As mentioned in the introduction, one of the objectives was to develop a procedure with the ability to calibrate other specimens with optimized performance. This can be done by using the results of the initial DEM simulations to fit other set of surrogate models in which the target variables are computed as the difference between the DEM results and those from another specimen. The results of the application of this procedure are shown in Fig. 15: they correspond to another clay specimen with different humidity (20.2%). The DEM calculations were reused by computing the errors between them and the new laboratory experiment for each point. The calibrated parameters obtained in this case are $E = 5.81$ MPa, $\mu = 0.27$, $c_0 = 19.33$ kPa and $k_c = 0.35$, that lead to a MAE equal to 2.90 kPa.

The results reveal that even reusing the DEM calculations, the calibration procedure provides accurate results. This is because both specimens are similar and the initial ranges selected are relatively wide. However, the error in the prediction can be reduced by adding more DEM simulations.

In this case, we took the values achieved after the 5th iteration of the calibration algorithm (admissible error $I_e/5 = 5$ kPa) and develop another series of 50 DEM calculations. Then, we fit new RF models with the enlarged training set (650 total runs). Figure 16 shows the results of the DEM calculation after the improved calibration. The material parameters obtained after the calibration procedure are

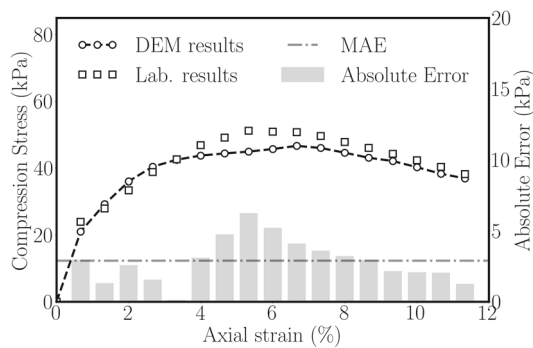


Fig. 15 DEM calculation of a clay sample with a 20.2% of humidity obtained after calibrating with $L_s = 1000$, $it_{\max} = 50$ and $I_e = 25$. Material parameters: $E = 5.81$ MPa, $\mu = 0.27$, $c_0 = 19.33$ kPa and $k_c = 0.35$. MAE = 2.90 kPa

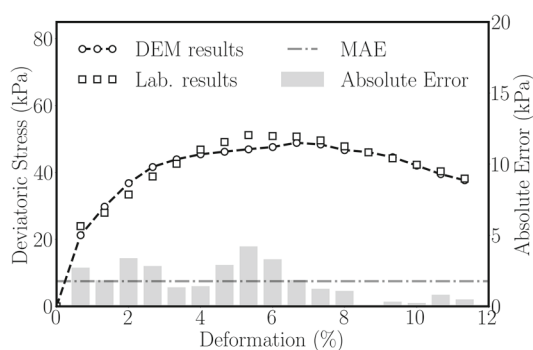


Fig. 16 DEM calculation of a clay sample with a 20.2% of humidity obtained after the improved calibration with: $L_s = 1000$, $it_{\max} = 50$ and $I_e = 25$. Material parameters: $E = 5.89$ MPa, $\mu = 0.27$, $c_0 = 20.16$ kPa and $k_c = 0.36$. MAE = 1.87 kPa

$E = 5.89$ MPa, $\mu = 0.27$, $c_0 = 20.16$ kPa and $k_c = 0.36$, with a MAE equal to 1.87 kPa.

The results of this last DEM calculation are shown together with the final state of the real sample in Fig. 17. They lead to the conclusion that the failure mechanism observed in the numerical model is consistent with that experienced in the laboratory.

5 Discussion

The proposed approach was successfully applied for calibrating seven parameters to reproduce the complete behaviour of two clay specimens along uniaxial compression tests, i.e. for 17 points in the stress–strain curve. It took less than one minute, while the development of the same amount of numerical DEM calculations that were evaluated with the proposed algorithm would take more than 5 years (in 16 Intel Xeon E5-2670 CPU processors). The overall strategy has thus shown to be effective for the case study considered.

In spite of that, and though the method was defined with the aim of being applicable to other settings, some important decisions need to be made to adapt the framework to different problems.

The amount of initial runs of the numerical model is highly relevant in the overall result. It has a major influence on the accuracy of the surrogate model, which in turn is essential in the overall outcome. Highly complex phenomena with many parameters to calibrate may require large training data sets for fitting an accurate surrogate model that may be costly to generate if the computational time for each simulation is high. The limitation of the method for complex and costly phenomena is associated to the numerical approach itself; the proposed method outperforms trial and error in any setting.

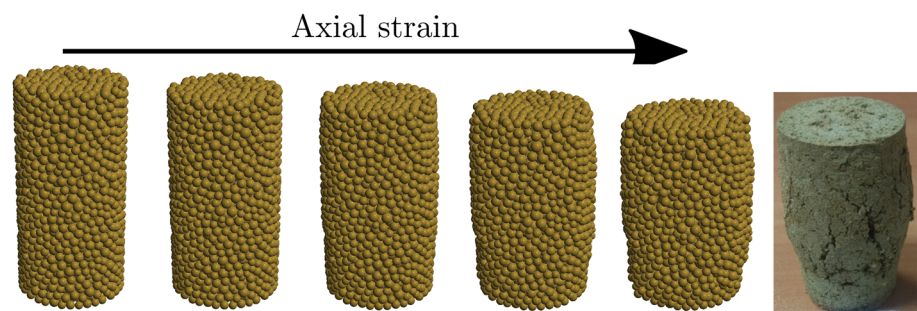
The high-level idea of iteratively reducing the admissible ranges of the parameters to calibrate can be applied together with different surrogate models and even with other numerical approaches. We chose to define the process by setting the initial error, which is reduced at each iteration. One advantage of this approach is that spurious, isolated combinations of parameters which might throw admissible results from the surrogate models are discarded automatically. The iterative process also contributes to the computational efficiency of the process.

The choice of the algorithm for the surrogate model is also important. RF are particularly suited for problems with relatively high number of inputs (parameters to calibrate in this case), but the main advantage observed from our experience is the simplicity of the fitting process and the robustness of the algorithm. While the tuning process requires relevant efforts for algorithms such as NNs (number of layers, number of neurons per layer, training algorithm and associated parameters need to be defined), default training parameters offer accurate RF models in many settings. In the case study considered, preliminary computations allowed verifying the minor effect of the number of trees and the number of variables to evaluate at each split in the RF model accuracy. This simplicity allows its application without the need for a profound background in ML to tune the RF model.

The automatic calculation of the importance of the variables in RF models can also make a difference as compared to other algorithms. In the case studied, a preliminary set of 100 calculations has been carried out. Although the RF model with this data set was not particularly precise (for some outputs, the OOB R^2 score was lower than 70%), it allowed us to evaluate the variable importance, remove those with low influence, and run 600 new cases with just four parameters, leading to a RF model with a much higher accuracy.

Other possibility for optimizing the process involves generating training data sets of increasing size until some degree of accuracy of the surrogate model is achieved. In this regard, RF offer an additional advantage, since a good estimate of the model accuracy can be computed from the OOB data, with-

Fig. 17 Evolution of the sample in the DEM calculation with increasing axial strain and comparison with the experiment



out the need to reserve a dedicated validation set or to do cross-validation of related techniques. This option requires a modification of the sampling strategy to preserve the properties of the data set as size increases, using for instance the Progressive Latin Hypercube Sampling [63]. Alternatively, the intermediate ranges generated can also be used to perform further numerical simulations and refine the model.

The interpretation of the RF model can also provide insights on the physical phenomenon and on how the DEM model is reproducing the behaviour of the material. Although not directly related to the calibration process, the analysis of the evolution of the variable importance along the test can be useful to verify the appropriateness of the contact model used or of other elements of the DEM model.

The same approach can also be used for calibrating other parameters involved in the DEM model, in addition to those associated to the contact law. Although it adds complexity to the overall problem, other elements such as the particle size or the time step can be calibrated with this method. Likewise, since the method was focussed on vector QoIs, it can be used in problems where tests of different nature are performed on a given material.

6 Conclusions

In this work, an automatic algorithm for the calibration of DEM parameters was proposed. It was developed at high-level, with the aim of being applicable to other settings: different numerical approaches, surrogate models, materials and physical phenomena. It is based on ML techniques and has the capability of calibrating the properties of the material for scalar and multiple outcomes. Its design allows also to reuse the results of a previous DEM simulations for calibrating similar materials.

To successfully conduct the calibration procedure, several considerations shall be taken into account: a) the parameters to calibrate and their initial ranges, b) the number of DEM calculations to run for fitting the surrogate model, c) the training process of the surrogate model and d) the three parameters that control the iterative algorithm (L_s , I_e and it_{\max}).

The effect on the accuracy of the results of the three parameters that control the procedure is minor as well as on the overall computational time. The most important verification to make is that the initial ranges are wide enough to encompass the calibrated values. Additionally, different weights can be assigned to each element in the vector QoI to focus on some part of the stress–strain curve (in the case study considered) or on some particular indicator of the behaviour of the material.

The algorithm was tested for the calibration of seven material properties defining a cohesive DEM contact model to reproduce the behaviour of one clay sample under uniaxial compression test. The final calibrated parameters were plug into the DEM model, and the strain–stress curve was reproduced with an average error of 2.08 kPa. The same process with the same initial DEM simulations was applied to another specimen of the same material with different humidity. The average error increased to 2.90 kPa, but decreased up to 1.87 kPa just with 50 additional DEM simulations.

The results obtained suggest that the proposed procedure can be useful in other settings, as well as for calibrating other elements of the model, in addition to the parameters of the contact law.

Acknowledgements This work was partially funded by the Spanish Ministry of Science, Innovation and Universities through the Project TRISTAN (RTI2018-094785-B-I00) financed by MCIN/AEI/10.13039/501100011033/ and FEDER *Una manera de hacer Europa*. The authors also acknowledge financial support from the Spanish Ministry of Economy and Competitiveness, through the Severo Ochoa Programme for Centres of Excellence in R&D (CEX2018-000797-S) and from the Generalitat de Catalunya through the CERCA Programme. Also, the authors would like to acknowledge Dr. Ricardo Alves for providing the data sets from the experiments carried out in Technical University of Madrid.

Declarations

Conflict of interest On behalf of all authors, the corresponding author states that there is no conflict of interest.

References

1. AENOR (1993) Simple compression rupture test in soil test specimens; UNE 103400:1993. techreport, AENOR

2. Baranau V, Tallarek U (2014) Random-close packing limits for monodisperse and polydisperse hard spheres. *Soft Matter* 10(21):3826–3841. <https://doi.org/10.1039/C3SM52959B>
3. Benvenuti L, Kloss C, Pirker S (2016) Identification of DEM simulation parameters by artificial neural networks and bulk experiments. *Powder Technol* 291:456–465. <https://doi.org/10.1016/j.powtec.2016.01.003>
4. Boikov AV, Savelev RV, Payor VA (2018) DEM calibration approach: design of experiment. *J Phys Conf Ser* 1015:032017. <https://doi.org/10.1088/1742-6596/1015/3/032017>
5. Boikov AV, Savelev RV, Payor VA (2018) DEM calibration approach: random forest. *J Phys Conf Ser* 1118:012009. <https://doi.org/10.1088/1742-6596/1118/1/012009>
6. Bowles J (2001) *Foundation analysis and design*. McGraw Hill, New York
7. Breiman L (2001) Random forests. *Mach Learn* 45(1):5–32. <https://doi.org/10.1023/A:1010933404324>
8. Breiman L, Friedman JH, Olshen RA, Stone CJ (2017) *Classification and regression trees*. Routledge, New York
9. Brown NJ, Chen JF, Ooi JY (2014) A bond model for DEM simulation of cementitious materials and deformable structures. *Granul Matter* 16(3):299–311. <https://doi.org/10.1007/s10035-014-0494-4>
10. Caruana R, Niculescu-mizil A (2006) An empirical comparison of supervised learning algorithms. In: *Proceedings. 23rd international conference. Machine learning (ICML'06)*, pp. 161–168
11. Cheng H, Shuku T, Thoeni K, Tempone P, Luding S, Magnanimo V (2019) An iterative Bayesian filtering framework for fast and automated calibration of DEM models. *Comput Methods Appl Mech Eng* 350:268–294. <https://doi.org/10.1016/j.cma.2019.01.027>
12. Chinesta F, Cueto E, Klusemann B (2021) Empowering materials processing and performance from data and AI. *Materials (Basel)* 14(16):4409. <https://doi.org/10.3390/ma14164409>
13. Coetzee CJ (2017) Review: calibration of the discrete element method. *Powder Technol* 310:104–142. <https://doi.org/10.1016/j.powtec.2017.01.015>
14. Coetzee CJ (2019) Particle upscaling: calibration and validation of the discrete element method. *Powder Technol* 344:487–503. <https://doi.org/10.1016/j.powtec.2018.12.022>
15. Cundall PA, Hart RD (1992) Numerical modelling of discontinua. *Eng Comput* 9(2):101–113. <https://doi.org/10.1108/eb023851>
16. Cundall PA, Strack ODL (1979) A discrete numerical model for granular assemblies. *Géotechnique* 29(1):47–65
17. Dadvand P, Rossi R, Onate E (2010) An object-oriented environment for developing finite element codes for multi-disciplinary applications. *Arch Comput Methods Eng* 17(3):253–297. <https://doi.org/10.1007/s11831-010-9045-2>
18. De Pue J, Di Emidio G, Verastegui Flores RD, Bezuijen A, Cornelis WM (2019) Calibration of DEM material parameters to simulate stress-strain behaviour of unsaturated soils during uniaxial compression. *Soil Tillage Res* 194:104303. <https://doi.org/10.1016/j.still.2019.104303>
19. Derjaguin BV, Muller VM, Toporov YP (1975) Effect of contact deformations on the adhesion of particles. *J Colloid Interface Sci* 53(2):314–326. [https://doi.org/10.1016/0021-9797\(75\)90018-1](https://doi.org/10.1016/0021-9797(75)90018-1)
20. Desai PS, Mehta A, Dougherty PSM, Higgs CF (2019) A rheometry based calibration of a first-order DEM model to generate virtual avatars of metal additive manufacturing (AM) powders. *Powder Technol* 342:441–456. <https://doi.org/10.1016/j.powtec.2018.09.047>
21. Do HQ, Aragón AM, Schott DL (2018) A calibration framework for discrete element model parameters using genetic algorithms. *Adv Powder Technol* 29(6):1393–1403. <https://doi.org/10.1016/j.apt.2018.03.001>
22. El-Kassem B, Salloum N, Brinz T, Heider Y, Markert B (2021) A multivariate regression parametric study on DEM input parameters of free-flowing and cohesive powders with experimental data-based validation. *Comput Part Mech* 8(1):87–111. <https://doi.org/10.1007/s40571-020-00315-8>
23. Fakhimi A, Villegas T (2006) Application of dimensional analysis in calibration of a discrete element model for rock deformation and fracture. *Rock Mech Rock Eng* 40(2):193. <https://doi.org/10.1007/s00603-006-0095-6>
24. Fathipour-Azar H (2021) Machine learning-assisted distinct element model calibration: ANFIS, SVM, GPR, and MARS approaches. *Acta Geotech*. <https://doi.org/10.1007/s11440-021-01303-9>
25. Feng YT, Han K, Owen DRJ, Loughran J (2009) On upscaling of discrete element models: similarity principles. *Eng Comput* 26(6):599–609. <https://doi.org/10.1108/02644400910975405>
26. Grobbel J, Brendelberger S, Henninger M, Sattler C, Pitz-Paal R (2020) Calibration of parameters for DEM simulations of solar particle receivers by bulk experiments and surrogate functions. *Powder Technol* 364:831–844. <https://doi.org/10.1016/j.powtec.2019.11.028>
27. Hanley KJ, O'Sullivan C, Oliveira JC, Cronin K, Byrne EP (2011) Application of Taguchi methods to DEM calibration of bonded agglomerates. *Powder Technol* 210(3):230–240. <https://doi.org/10.1016/j.powtec.2011.03.023>
28. Hariri-Ardebili MA, Salazar F (2020) Engaging soft computing in material and modeling uncertainty quantification of dam engineering problems. *Soft Comput* 24(15):11583–11604. <https://doi.org/10.1007/s00500-019-04623-x>
29. Harkness J, Zervos A, Le Pen L, Aingaran S, Powrie W (2016) Discrete element simulation of railway ballast: modelling cell pressure effects in triaxial tests. *Granul Matter* 18(3):65
30. Hartmann P, Cheng H, Thoeni K (2022) Performance study of iterative Bayesian filtering to develop an efficient calibration framework for DEM. *Comput Geotech* 141:104491. <https://doi.org/10.1016/j.compgeo.2021.104491>
31. Hassanzadeh V, Wensrich CM, Moreno-Atanasio R (2020) Elucidation of the role of cohesion in the macroscopic behaviour of coarse particulate systems using DEM. *Powder Technol* 361:374–388. <https://doi.org/10.1016/j.powtec.2019.07.070>
32. Hengl T, Nussbaum M, Wright MN, Heuvelink GBM, Graler B (2018) Random forest as a generic framework for predictive modeling of spatial and spatio-temporal variables. *PeerJ* 6:e5518. <https://doi.org/10.7717/peerj.5518>
33. Hlosta J, Jezerská L, Rozbroj J, Žurovec D, Nečas J, Zegzulka J (2020) DEM investigation of the influence of particulate properties and operating conditions on the mixing process in rotary drums: part-determination of the DEM parameters and calibration process. *Processes* 8(2):222. <https://doi.org/10.3390/pr8020222>
34. Ho TK (1995) Random decision forests. In: *Proceedings of the third international conference on document analysis and recognition—Volume 1, ICDAR '95*, p. 278. IEEE Computer Society, USA
35. Hsieh YM, Li HH, Huang TH, Jeng FS (2008) Interpretations on how the macroscopic mechanical behavior of sandstone affected by microscopic properties—Revealed by bonded-particle model. *Eng Geol* 99(1):1–10. <https://doi.org/10.1016/j.enggeo.2008.01.017>
36. Ibrahim M (2020) An empirical comparison of random forest-based and other learning-to-rank algorithms. *Pattern Anal Appl* 23(3):1133–1155. <https://doi.org/10.1007/s10044-019-00856-6>
37. Indraratna B, Ngo NT, Rujikiatkamjorn C, Vinod JS (2014) Behavior of fresh and fouled railway ballast subjected to direct shear testing: discrete element simulation. *Int J Geomech* 14(1):34–44. [https://doi.org/10.1061/\(ASCE\)GM.1943-5622.0000264](https://doi.org/10.1061/(ASCE)GM.1943-5622.0000264)
38. Irazábal J, Salazar F, Oñate E (2017) Numerical modelling of granular materials with spherical discrete particles and the bounded rolling friction model. Application to railway ballast. *Comput Geotech* 85:220–229. <https://doi.org/10.1016/j.compgeo.2016.12.034>

39. Irazábal J, Salazar F, Santasusana M, Oñate E (2019) Effect of the integration scheme on the rotation of non-spherical particles with the discrete element method. *Comput Part Mech* 6(4):545–559. <https://doi.org/10.1007/s40571-019-00232-5>
40. James G, Witten D, Hastie T, Tibshirani R (2013) Tree-based methods. In: James G, Witten D, Hastie T, Tibshirani R (eds) *An introduction to statistical learning: with applications in R*, Springer texts in statistics. Springer, New York, pp 303–335
41. Johnson KL, Kendall K, Roberts AD, Tabor D (1971) Surface energy and the contact of elastic solids. *Proc R Soc Lond A Math Phys Sci* 324(1558):301–313. <https://doi.org/10.1098/rspa.1971.0141>
42. Joseph VR, Hung Y (2008) Orthogonal-maximin latin hypercubes designs. *Stat Sin* 18(1):171–186
43. Karkala S, Davis N, Wassgren C, Shi Y, Liu X, Riemann C, Yacobian G, Ramachandran R (2019) Calibration of discrete-element-method parameters for cohesive materials using dynamic-yield-strength and shear-cell experiments. *Processes* 7(5):278. <https://doi.org/10.3390/pr7050278>
44. Lommen S, Mohajeri M, Lodewijks G, Schott D (2019) DEM particle upscaling for large-scale bulk handling equipment and material interaction. *Powder Technol* 352:273–282. <https://doi.org/10.1016/j.powtec.2019.04.034>
45. Mahmood AA, Elektorowicz M (2016) A review of discrete element method research on particulate systems. *IOP Conf Ser Mater Sci Eng* 136:012034. <https://doi.org/10.1088/1757-899X/136/1/012034>
46. Maw N, Barber JR, Fawcett JN (1976) The oblique impact of elastic spheres. *Wear* 38(1):101–114. [https://doi.org/10.1016/0043-1648\(76\)90201-5](https://doi.org/10.1016/0043-1648(76)90201-5)
47. Meier C, Weissbach R, Weinberg J, Wall WA, John Hart A (2019) Modeling and characterization of cohesion in fine metal powders with a focus on additive manufacturing process simulations. *Powder Technol* 343:855–866. <https://doi.org/10.1016/j.powtec.2018.11.072>
48. Mohajeri MJ, Do HQ, Schott DL (2020) DEM calibration of cohesive material in the ring shear test by applying a genetic algorithm framework. *Adv Powder Technol* 31(5):1838–1850. <https://doi.org/10.1016/j.apt.2020.02.019>
49. Monteiro Alves RM (2021) Proceso de rotura de las presas de escollera por sobrevertido. phd, E.T.S.I. Caminos, Canales y Puentes (UPM)
50. Navarro HA, de Souza Braun MP (2013) Determination of the normal spring stiffness coefficient in the linear spring-dashpot contact model of discrete element method. *Powder Technol* 246:707–722. <https://doi.org/10.1016/j.powtec.2013.05.049>
51. Oñate E, Zárate F, Miquel J, Santasusana M, Celigueta MA, Arrufat F, Gandikota R, Valiullin K, Ring L (2015) A local constitutive model for the discrete element method. Application to geomaterials and concrete. *Comput Part Mech* 2(2):139–160. <https://doi.org/10.1007/s40571-015-0044-9>
52. Obermayr M, Vrettos C, Eberhard P, Däuwel T (2014) A discrete element model and its experimental validation for the prediction of draft forces in cohesive soil. *J Terramech* 53:93–104. <https://doi.org/10.1016/j.jterra.2014.04.003>
53. Orefice L, Khinast JG (2020) A novel framework for a rational, fully-automatised calibration routine for DEM models of cohesive powders. *Powder Technol* 361:687–703. <https://doi.org/10.1016/j.powtec.2019.11.054>
54. Pachón-Morales J, Do H, Colin J, Puel F, Perré P, Schott D (2019) DEM modelling for flow of cohesive lignocellulosic biomass powders: model calibration using bulk tests. *Adv Powder Technol* 30(4):732–750. <https://doi.org/10.1016/j.apt.2019.01.003>
55. Pedregosa F, Varoquaux G, Gramfort A, Michel V, Weiss R, Dubourg V, Vanderplas J, Passos A, Cournapeau D, Brucher M, Perrot M, Duchesnay E (2011) Scikit-learn: machine Learning in Python. *J Mach Learn Res* 12:2825–2830
56. Popov VL (2010) Coulomb's law of friction. In: Popov VL (ed) *Contact mechanics and friction: physical principles and applications*. Springer, Berlin, pp 133–154
57. Rackl M, Hanley KJ (2017) A methodical calibration procedure for discrete element models. *Powder Technol* 307:73–83. <https://doi.org/10.1016/j.powtec.2016.11.048>
58. Richter C, Rößler T, Kunze G, Katterfeld A, Will F (2020) Development of a standard calibration procedure for the DEM parameters of cohesionless bulk materials-Part II: efficient optimization-based calibration. *Powder Technol* 360:967–976. <https://doi.org/10.1016/j.powtec.2019.10.052>
59. Roessler T, Katterfeld A (2018) Scaling of the angle of repose test and its influence on the calibration of DEM parameters using upscaled particles. *Powder Technol* 330:58–66. <https://doi.org/10.1016/j.powtec.2018.01.044>
60. Roessler T, Katterfeld A (2019) DEM parameter calibration of cohesive bulk materials using a simple angle of repose test. *Particuology* 45:105–115. <https://doi.org/10.1016/j.partic.2018.08.005>
61. Santasusana M, Irazábal J, Oñate E, Carbonell JM (2016) The double hierarchy method. A parallel 3D contact method for the interaction of spherical particles with rigid FE boundaries using the DEM. *Comput Part Mech* 3(3):407–428. <https://doi.org/10.1007/s40571-016-0109-4>
62. Schulze D (2008) Practical determination of flow properties. In: Schulze D (ed) *Powders and bulk solids: behavior, characterization, storage and flow*. Springer, Berlin, pp 75–111
63. Sheikholeslami R, Razavi S (2017) Progressive latin hypercube sampling: an efficient approach for robust sampling-based analysis of environmental models. *Environ Model Softw* 93:109–126. <https://doi.org/10.1016/j.envsoft.2017.03.010>
64. Song C, Wang P, Makse HA (2008) A phase diagram for jammed matter. *Nature* 453(7195):629–632. <https://doi.org/10.1038/nature06981>
65. Thornton C, Cummins SJ, Cleary PW (2011) An investigation of the comparative behaviour of alternative contact force models during elastic collisions. *Powder Technol* 210(3):189–197. <https://doi.org/10.1016/j.powtec.2011.01.013>
66. Tran VDH, Meguid MA, Chouinard LE (2014) Discrete element and experimental investigations of the earth pressure distribution on cylindrical shafts. *Int J Geomech* 14(1):80–91
67. Valera RR, Morales IP, Vanmaercke S, Morfa CR, Cortés LA, Casañas HDG (2015) Modified algorithm for generating high volume fraction sphere packings. *Comput Part Mech* 2(2):161–172. <https://doi.org/10.1007/s40571-015-0045-8>
68. Westbrink F, Elbel A, Schwung A, Ding SX (2021) Optimization of DEM parameters using multi-objective reinforcement learning. *Powder Technol* 379:602–616. <https://doi.org/10.1016/j.powtec.2020.10.067>
69. Ye F, Wheeler C, Chen B, Hu J, Chen K, Chen W (2019) Calibration and verification of DEM parameters for dynamic particle flow conditions using a backpropagation neural network. *Adv Powder Technol* 30(2):292–301. <https://doi.org/10.1016/j.apt.2018.11.005>
70. Yoon J (2007) Application of experimental design and optimization to PFC model calibration in uniaxial compression simulation. *Int J Rock Mech Min Sci* 44(6):871–889. <https://doi.org/10.1016/j.ijrmms.2007.01.004>
71. Zhang P, Sun X, Zhou X, Zhang Y (2022) Experimental simulation and a reliable calibration method of rockfill microscopic parameters by considering flexible boundary. *Powder Technol* 396:279–290. <https://doi.org/10.1016/j.powtec.2021.10.061>
72. Zhang S, Tekeste MZ, Li Y, Gaul A, Zhu D, Liao J (2020) Scaled-up rice grain modelling for DEM calibration and the validation of hopper flow. *Biosyst Eng* 194:196–212. <https://doi.org/10.1016/j.biosystemseng.2020.03.018>

73. Zhou H, Hu Z, Chen J, Lv X, Xie N (2018) Calibration of DEM models for irregular particles based on experimental design method and bulk experiments. *Powder Technol* 332:210–223. <https://doi.org/10.1016/j.powtec.2018.03.064>
74. Zhou L, Chu X, Xu Y (2017) DEM investigation on characteristics of rolling resistance for modelling particle shape. *EPJ Web Conf* 140:05005. <https://doi.org/10.1051/epjconf/201714005005>
75. Zhu HP, Zhou ZY, Yang RY, Yu AB (2008) Discrete particle simulation of particulate systems: a review of major applications and findings. *Chem Eng Sci* 63(23):5728–5770

Publisher's Note Springer Nature remains neutral with regard to jurisdictional claims in published maps and institutional affiliations.

Springer Nature or its licensor (e.g. a society or other partner) holds exclusive rights to this article under a publishing agreement with the author(s) or other rightsholder(s); author self-archiving of the accepted manuscript version of this article is solely governed by the terms of such publishing agreement and applicable law.